Seismic Performance of Resilient Self-Centering Bridge Piers Equipped with SMA Bars

Sedef Kocakaplan[1], Ehsan Ahmadi[2], Mohammad M. Kashani[3]*
[1]Faculty of Engineering and Natural Sciences, Bursa Technical University, TR
[2]Faculty of Engineering and the Built Environment, Birmingham City University, UK
[3]Faculty of Engineering and Physical Sciences, University of Southampton, UK

** Corresponding Author, email: sedef.kocakaplan@btu.edu.tr*

Abstract

This study examines the seismic behavior of precast post-tensioned segmental (PPS) bridge piers that are equipped with Shape Memory Alloy (SMA) bars. PPS piers are designed to minimize overall and localized damage to bridges by incorporating natural hinges and rocking mechanisms. The introduction of super-elastic SMA bars has the potential to enhance the use of PPS piers in high-seismic regions. A parametric study is conducted to identify piers with the highest energy dissipation capacity, which are then subjected to dynamic analysis. The aim is to assess the energy dissipation capability of these systems by subjecting the selected piers, both with and without SMA bars, to far-field ground motions using a Finite Element (FE) framework. The seismic performance of the piers is evaluated using Incremental Dynamic Analysis (IDA) curves, which are obtained from analyzing the piers under 44 far-fault ground motions. The IDA results indicate a significant reduction in the drift responses of the piers when SMA bars are utilized.

Keywords: Resilience-based design; shape memory alloy; incremental dynamic analysis; seismic performance assessment

1. Introduction

Precast post-tensioned segmental (PPS) piers are resilient structures as the post-tensioning tendon running along the pier length provide self-centring mechanism ((Shim et al., 2008), (Dawood et al., 2012)). Further, rocking mechanism between the segments prevents the development of large concrete cracks and permanent plastic deformations. However, under earthquake loading, PPS piers behave without significant hysteresis, resulting in having low or no hysteretic damping ((Hewes and Priestley, 2002), (Roh and Reinhorn, 2010), (Marriott et al., 2009), (Billington and Yoon, 2004), (Motaref et al., 2014), (Tazarv and Saiid Saiidi, 2016),(Billington et al., 1999)). In order to increase the seismic performance and energy dissipation capacity of the precast post-tensioned segmental (PPS) bridge piers, different methods have been proposed (i.e, internal bars and external energy dissipating devices). To improve the energy dissipation capacity (Ou et al., 2010)), applied mild internal steel bars or energy dissipating (ED) bars across the piers' segments. The authors showed that the piers can exhibit a flag-shape behaviour with reduced residual drifts if the ratio of the ED bars is below a specific level. The use of external energy dissipation devices also performed. For instance, (Marriott et al., 2009) achieved an increase in the energy dissipation capacity of the PPS piers through the application of the external replaceable dissipaters. (Chou and Chen, 2006) also used external energy dissipaters as a 5-mm thick A36 Reduced Steel Plate (RSP) at the base of the columns as external dissipaters where the equivalent damping ratio of the entire system increased.

One alternative method to increase the dissipation capacity of the structures is the use of super-elastic Shape Memory Alloy (SMA) bars. SMA bars dissipates energy of the structure through their nonlinear deformations and return to their initial state after loading events (i.e., zero residual deformations). To investigate the energy dissipation capacity of SMA bars, many numerical and experimental studies have been conducted in recent years. Specifically, in bridge structures, the studies are performed for both cast-in-place (CIP) and PPS piers. For instance, (Varela and Saiid' Saiidi, 2014) numerically and experimentally studied use of super-elastic Copper Aluminium-Manganese (CuAlMn) SMA bars in the plastic hinge region of the CIP piers. The authors observed that with the use of SMA bars limited damage occurred at the plastic hinge region without compromising load-carrying capacity of the piers. Similarly, (Varela and 'Saiid' Saiidi, 2016) presented a resilient precast bridge column provided by super-elastic SMA bars and cementitious composite at the base of the column. The bridge piers are tested, and analytical models are analysed for two different types of SMA bar, one made of nickel-titanium and the other of copper aluminium-manganese. The study showed that the design of the bridge with advanced materials and detailing resulted in minimized damage to the critical zone of bridge columns and both of SMA bars were successful in recentring the columns. An example of SMA bars for PPS piers is using them at the base segment of the piers; for instance, (Moon et al., 2015), (Roh and Reinhorn, 2010) investigated seismic performance of the PPS piers using unbonded martensitic NiTi SMA, while (Nikbakht et al., 2015) studied application of SMA bars in PPS piers with steel jacketing tubes.

1.1. Research Contribution and Novelty

Although the detailing and performance of PPS piers with energy dissipation devices have been extensively studied, a comprehensive parametric investigation into the nonlinearity and seismic behaviour of PPS piers with SMA bars under both static and dynamic loads remains unexplored. The objective of this study is to examine the seismic performance of piers equipped with SMA bars using a Finite Element (FE) framework, which is validated against experimental results from Ahmadi and Kashani (2020). In addition, the authors have developed a new material model for SMA and incorporated it into OpenSees (McKenna, 2011) based on the work of Li et al. (2017). The ultimate goal is to develop a damage-resistant pier that incorporates SMA bars, thereby enhancing its resilience to seismic events. In this study, to increase the energy dissipation of the piers, SMA bars are used at the edge of the segments. The nonlinear behaviour of the piers is assessed through Incremental Dynamic Analysis (IDA). The remaining sections of the paper are structured as follows: Section 2 introduces the numerical model of the piers and SMA bars, outlining their characteristics and parameters. In Section 3, the ground motion database is described, along with the scaling approach employed for the ground motions utilized in the study. Section 4 focuses on the numerical analysis and presents a detailed discussion of the obtained results. This section specifically investigates the impact of SMA bars on the performance of PPS piers through a parametric study, identifying piers with the highest energy dissipation capacity. Finally, Section 5 offers a summary of the findings and presents the conclusions drawn from the study.

2. Finite Element Model

The 2D model of the bridge pier, considering the importance of the lateral modes (Ahmadi and Kashani, 2020; Lee and Billington, 2010), is created using the finite element analysis software OpenSees (McKenna, 2011). The schematic representation of the numerical model is illustrated in Figure 1. The various components of the model are explained in the subsequent sections as follows.

2.1. PPS Piers

This study considers PPS piers with varying aspect ratios. Figure 1a illustrates an example pier with a length of H=2000 mm. All piers, regardless of aspect ratio, are composed of precast concrete segments measuring 500 mm in width (B) and 500 mm in height (h). Importantly, with increase of aspect ratio or the slenderness of the piers, stability of the piers decreases as pointed out by Ahmadi and Kashani, 2020. These concrete segments are connected through a stainless steel post-tensioned (PT) tendon that runs along the length of the pier. The PT tendon provides a self-centring mechanism, enabling the pier to return to its original position after experiencing lateral loads. As shown in Figure 1a the bridge deck on top of the segments is modelled as a lumped mass. To enhance the energy dissipation capacity of the piers, super-elastic NiTi SMA bars are incorporated into the bottom segments of the piers. These SMA bars are post-tensioned and unbounded, as shown in Figure 1a.

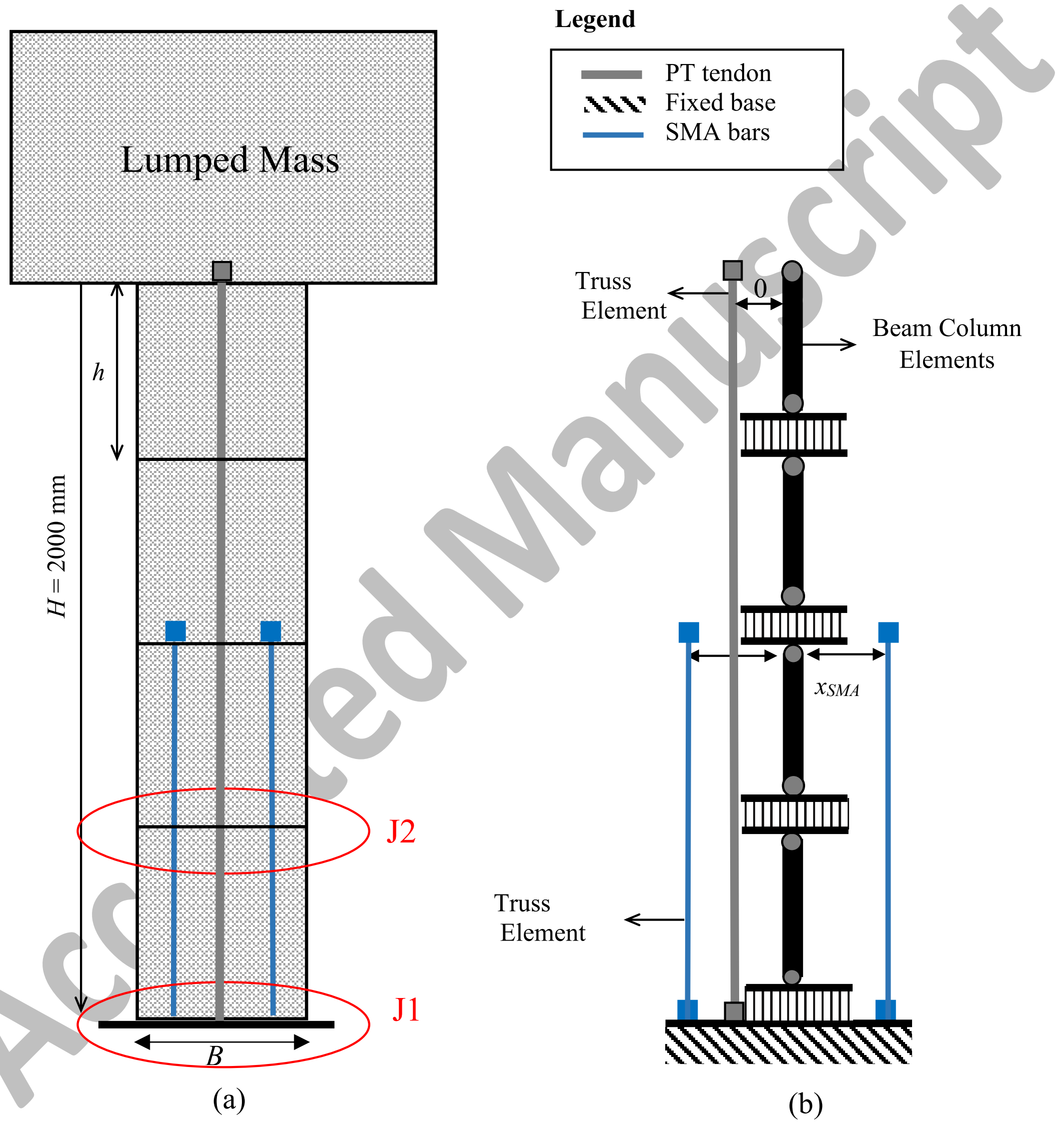

Figure 1. The PPS Pier with (a) dimensions, and (b) FE modeling

The FE analysis is performed based on the model proposed and experimentally validated in Ahmadi and Kashani, 2020 (see Figure 1b). Each concrete segment is modeled via Elastic Beam-Column elements with no sliding behavior. The stainless-steel PT tendon is modeled through the Truss elements with an Elastic Perfectly Plastic material. Yield stress, σ_y, and elastic modulus of the tendon are 1860 MPa and 200 GPa respectively. The material model includes the post-tensioning effect of the tendon which is defined as post-tensioning-to-yield stress, σ_t/σ_y. The geometric nonlinearities are also included in the model through Corotational geometric transformation for Beam-Column and Truss elements. Importantly, inertial effects of the bridge deck are included in the analysis by the application of lumped horizontal and vertical masses at the top node of the pier. The masses are equivalent to the axial force acting on the pier in which the axial load from the corresponding top deck is specified as the ratio of the axial load to axial capacity of the concrete section, $N/(f_c A_g)$. Here, N is the axial load, f_c and A_g are the concrete compressive strength (is defined as 35 MPa in this study) and the total cross section area of the segment, respectively.

Figure 1b also includes a schematic and details of the compression zones defined in the FE models. Each compression zone was modelled with a set of axial zero-length spring elements with an elastic zero-tension uniaxial material model to simulate the joint openings and compression forces at the contact surfaces. The vertical stiffness of the segments over the compression zones at the rocking joints of the piers was distributed by adopting the Lobatto Quadrature method. Readers are referred to (Ahmadi and Kashani, 2020) for the further details of the developed FE models.

2.2. SMA bars

The super-elastic shape memory alloy (SMA) bars are used in this study at the edge of the segments to increase the energy dissipation capacity of the entire pier. It is well known through many experimental and numerical studies that ((Leitner and Hao, 2016), (Shrestha and Hao, 2016), (Gao et al., 2016), (Suhail et al., 2020)) SMA bars can experience large strain and recover to its original shape through stress removal (super-elastic effect) or heating (shape memory effect) and provide large energy dissipation through the hysteretic behaviour ((Li et al., 2017), (Wilson and Wesolowsky, 2005), (DesRoches and Delemont, 2002), (Gholampour and Ozbakkaloglu, 2018)). The self-centering capability of the SMA also provides additional self- centering mechanism to PPS piers and provides piers to recover their original position after an earthquake with reducing the residual deformation of the structures.

SMA bars included in the FE models by using Truss Elements. The idealized constitutive model used for the SMA is presented in Figure 2. The tension and compression behavior of the SMAs are modelled as identical since the concerned behavior is the tension one. It can also be observed that the SMA can recover its original shape after unloading, which signifies being a self-centered material. The material properties in this work are based on the (Li et al., 2017) and the parameters are given in Table 1. Post-tensioning ratio of the SMA bars, α_{SMA}, is defined as $\sigma_{SMA}{}^{0}/\ \sigma_{sAM}$, where $\sigma_{SMA}{}^{0}$ is the initial post-tensioning stress in SMA bars, and σ_{sAM} is the start stress at austenite-to-martensite transformation phase, σ_{sAM} (see Table 1 and Figure 2). The SMA material model with initial post-tensioning stress was coded and implemented in OpenSees by the authors.

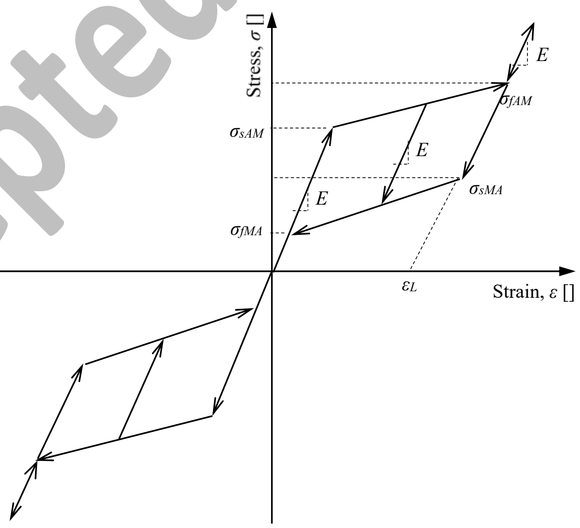

Figure 2. Idealized constitutive model of SMA material implemented by the authors in OpenSees.

Table 1. SMA parameters used in this study (Li et al., 2017).

Parameters	Description	Value
E	Initial modulus of elasticity	68.2 GPa
ε_L	Volumetric transformation strain	0.06
σ_{sAM}	Start stress at austenite-to-martensite transformation phase	480 MPa
σ_{fAM}	Finish stress at austenite-to-martensite transformation phase	540 MPa
σ_{sMA}	Start stress at martensite-to-austenite transformation phase	260 MPa
σ_{fMA}	Finish stress at martensite-to-austenite transformation phase	120 MPa

3. The Ground Motion Database

For this study, a set of 44 far-fault ground motion records, recommended in FEMA P659 (Applied Technology Council, 2009), is utilized. These records consist of 22 pairs of horizontal ground motions obtained from sites located at a distance greater than 10 km from the fault rupture. In the Appendix, Table 1 provides further details. Each strong ground motion within the dataset exhibits a peak ground acceleration (PGA) exceeding 0.2 g. Additionally, the peak ground velocity (PGV) for all strong ground motions is larger than 15 cm/s. These ground motions were recorded at sites characterized by soft rock and stiff soil conditions (site class C and D) as well as shallow crustal sources.

4. Analyses, results, and discussion

Prior to conducting the seismic performance analysis of the piers, a parametric study is conducted using nonlinear static analysis. The aim of this study is to determine the maximum energy capacity of PPS piers equipped with SMA bars. Several design parameters are investigated, which play a crucial role in controlling the energy dissipation capacity of the piers. These parameters include: (*i*) number of segments or aspect ratio, (*ii*) length, area, and post-tensioning ratio of the SMA bars, and (*iii*) area and the post-tensioning ratio of the tendon.

4.1. Parametric Study

The influence of the design parameters given in Table 2 are investigated in the present study to perform nonlinear static analysis of the piers. The same numerical model is used for all the cases by adjusting different design parameters for the reference columns. The capacity curves are obtained for a full cyclic loop (± 6 % drift) for the design parameters and the loading protocol is presented in Figure 3. According to Table 2, α_t is the post-tensioning ratio of the tendon (σ_T /σ_{Ty}) and and α_{sma} is the post-tensioning ratio of the SMA bars (σ_{sAM} /σ_{SAMy}) respectively; ρ_t is the tendon-to-segment area ratio (A_t/A_c), and ρ_{sma} is the SMA bars-to-segment area ratio (A_{sma}/A_c); n is the number of segments; and J_{sma} is the joint number at which the top node of the SMA bars is located. As shown in Figure 1a, the bottom end of all SMA bars is connected to the fixed base, and the top end location of the SMA bars varies and is shown by J_{sma}. So, J_{sma} represents different lengths of the SMA bars. The axial load ratio, $N/(f_cA_c)$, is taken 0.2 for all the analyses.

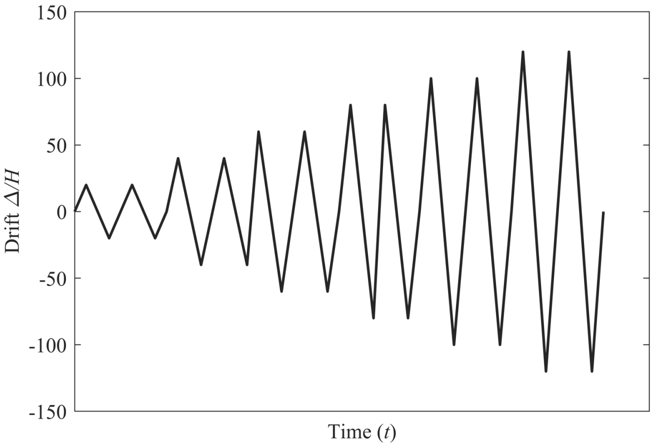

Figure 3. Applied loading protocol.

Figure 4 demonstrates the impact of the SMA bar area on the static behavior of the example pier with a segment count of n=4, considering different values of J_{sma} (representing the length of SMA bars). For this example, the post-tensioning ratio of tendon is taken as $\alpha_t = 0.4$, while tendon-to-segment area ratio, *is* $\rho_t = 0.015$, and post-tensioning ratio of SMA bar is $\alpha_{sma} = 0.3$. Here, drift response represents the ratio of the lateral displacement (Δ) at the joint level to the pier's height (*H*), while shear response is normalised by total weight (*W*) of the pier. It is observed that piers with ρ_{sma} = 0.025 (as shown in Figures 4(b) and 4(c)) exhibit the highest energy dissipation capacity compared to other piers. However, when J_{sma}=2 and a larger SMA bar area (ρ_{sma}=0.025) is used, the pier exhibits no energy dissipation (as seen in Figure 4(a)). This occurs because the SMA bars become very stiff for higher values of ρ_{sma} and smaller J_{sma}, leading to limited energy dissipation capabilities.

Table 2. Values of design parameters

Design Parameters						
n	$N/(f_c A_c)$	α_t	ρ_t	J_{sma}	α_{sma}	ρ_{sma}
2	0.2	0.0	0.010	2	0.0	0.005
4	0.2	0.2	0.015	3	0.3	0.01
6	0.2	0.4	0.020	4	0.6	0.015
10	0.2	0.6	-	5	-	0.025

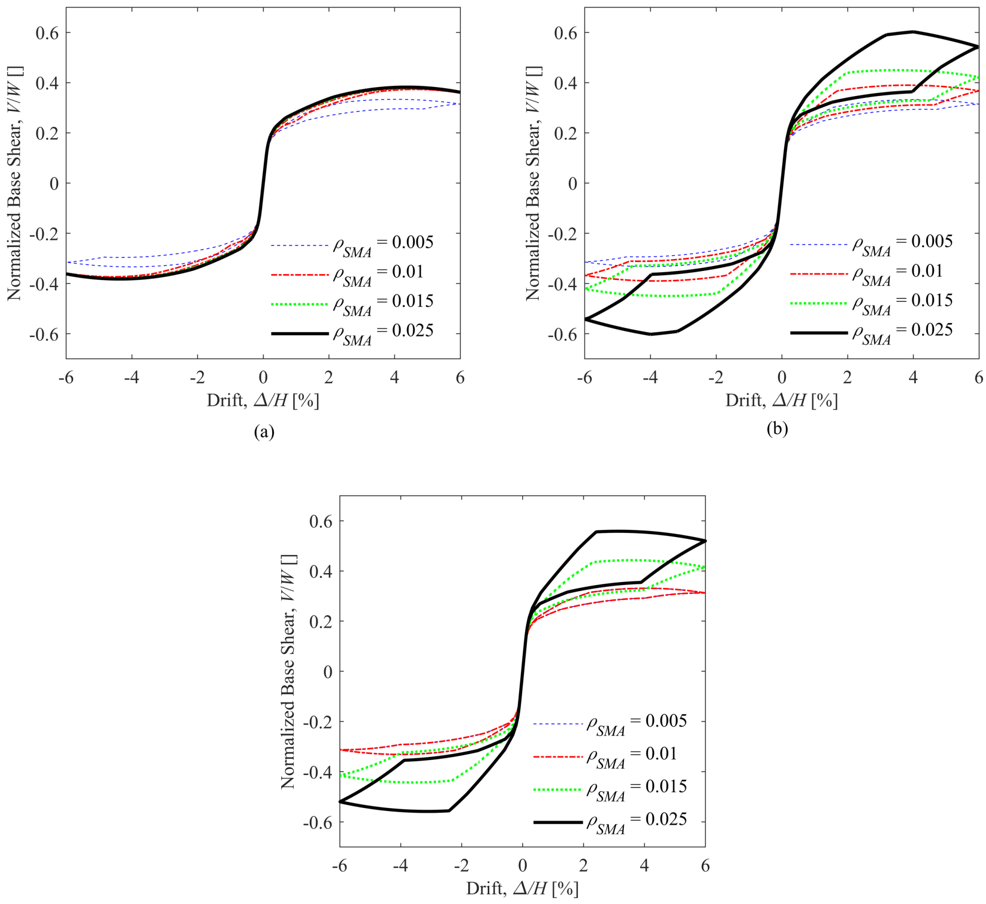

(a)

(b)

(c)

Figure 4. Effects of SMA bar area on pier with n=4, α_t=0.4, ρ_t=0.015, and α_{sma}=0.3 (a) J_{sma} =2; (b) J_{sma} = 3; (c) J_{sma}= 4

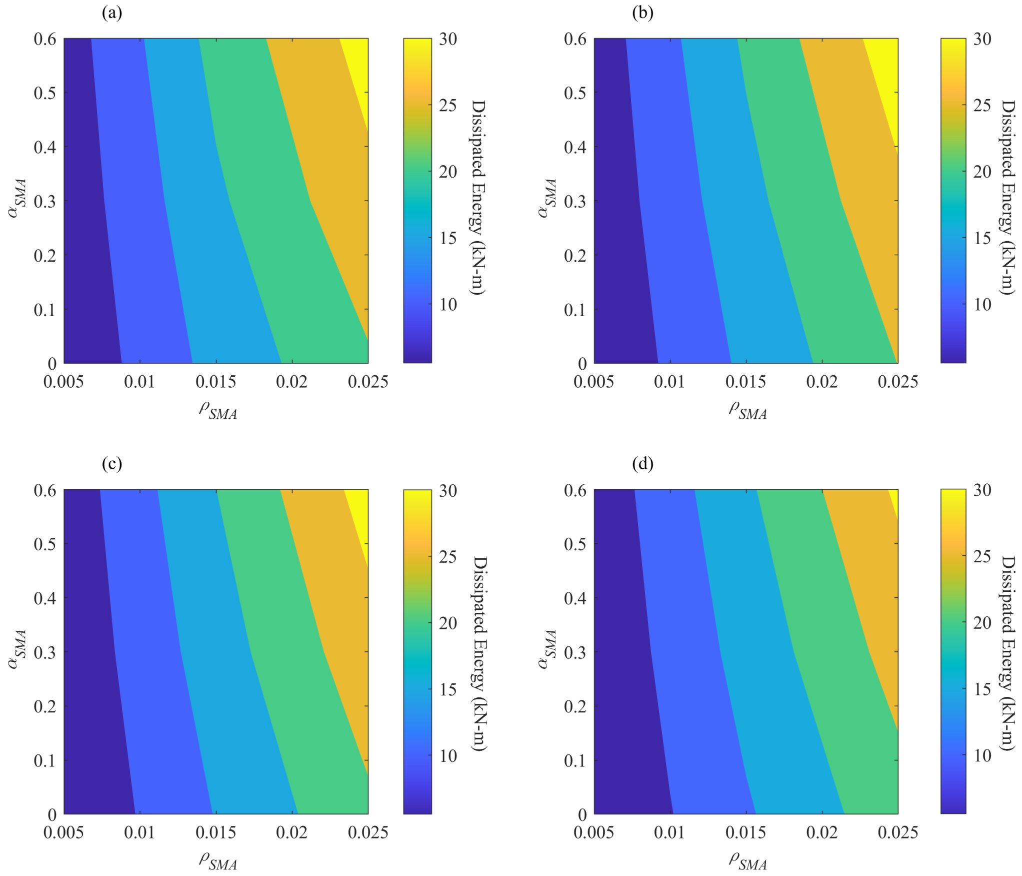

Figure 5. Dissipated energy of the exemplary pier ($n = 4$, $\rho_t = 0.015$, $J_{sma} = 3$) for: (a) $\alpha_t = 0.0$, (b) $\alpha_t = 0.2$, (c) $\alpha_t = 0.4$ and (d) $\alpha_t = 0.6$.

The outcome of the parametric study is utilized to analyze the effects of the design parameters on the energy dissipation of the piers. To assess this, the area enclosed by the cyclic behavior of the piers (base shear vs. drift) is calculated. This area is then considered as an indicator of the energy dissipated by the pier. By quantifying and comparing the areas enclosed by the cyclic behavior for different design parameter configurations, the study aims to determine the influence of these parameters on the energy dissipation capacity of the piers. An illustration of the contour plots for the dissipated energy for an exemplary pier with $\rho_t = 0.015$ and $J_{sma} = 3$ is illustrated in Figure 5 and details are presented in Kocakaplan et al., 2023. The amount of the dissipated energy is determined for a range of SMA's post-tensioning ratios, α_{SMA}, and SMA bar's area ratios, ρ_{sma}. Using the results of the contour plots, six piers are selected to be used in the dynamic analyses in the next section (section 4.2). Table 3 presents six piers, including their counterparts without SMA bars, along with their respective characteristics. Additionally, the first natural frequency of the piers, denoted as f_n, is provided. These frequency values are found to be very similar, indicating that the presence of the tendon and SMA bars has a negligible effect on the initial stiffness of the piers. This observation emphasizes that the primary influence of the tendon and SMA bars is related to the energy dissipation capacity of the piers, rather than affecting their initial stiffness. These frequency values will be utilized in Section 4.3 for further analysis.

Table 3. Representative piers for dynamic analyses

Piers	α_t	ρ_t	α_{sma}	ρ_{sma}	f_n (Hz)
A0	0.6	0.020	0.0	0.0	3.80
A1	0.6	0.020	0.6	0.025	3.96
A2	0.6	0.020	0.3	0.025	3.96
B0	0.4	0.020	0.0	0.00	3.80
B1	0.4	0.020	0.3	0.025	3.95
B2	0.4	0.020	0.6	0.025	3.95
C0	0.2	0.020	0.0	0.00	3.80
C1	0.2	0.020	0.6	0.025	3.96
C2	0.2	0.020	0.3	0.025	3.96

4.2. IDA Analysis

In this section, Incremental Dynamic Analysis (IDA) is conducted to explore the seismic performance of PPS piers equipped with SMA bars, and the results are compared with those obtained from piers without SMA bars. The IDA analyses were conducted to assess how the piers respond to various ground motion intensities, aiming to evaluate their seismic performance. The chosen intensity measure (IM) for the dynamic analysis is defined as the 5% damped spectral acceleration response at the first mode period of the piers, denoted as S_a (T_1, 5%). The first mode period (T_1) corresponds to the natural vibration period of the pier under very low-amplitude dynamic excitations, where the joints remain close, and no rocking motion is initiated. To determine the first period of the piers, an eigenvalue analysis is performed, and the resulting values are presented in Table 3 for each pier configuration. These period values will be utilized in the IDA to evaluate the seismic performance of the piers.

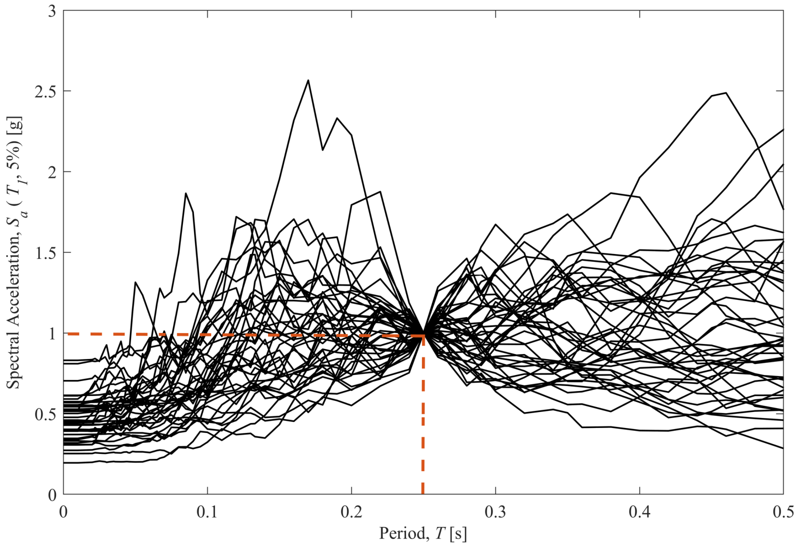

Figure 6. The scaled ground motion to 1 g at the first period of the pier

Prior to conducting the IDA analysis for each pier, the ground motions are first scaled to 1 g at the natural period of each pier using their 5% damped spectra as shown in Figure 6. Following the scaling, the IM is changed from 0.05 g to 1 g with the increment of 0.05 g. A small IM value of 0.005 g very close to 0 is also considered to ensure elastic behavior of the piers before their rocking initiation (Ahmadi et al., 2022; Ahmadi and Kashani, 2021).

4.3. IDA Curves

The result of the dynamic analysis is used to extract the IDA curves for the piers given in Table 3. The IDA curves are obtained through determining maximum values of time history responses of the piers for each record and IM value. Then, the IM values are plotted versus maximum responses. In this study, drift, relative rotation, shear force, and moment at joint levels of the segments are considered as seismic responses. Here, drift response represents the ratio of the lateral displacement (Δ) at the joint level to the pier's height (H), while shear and moment responses are normalised by total weight (W) of the pier, and its gravitational moment, represented by the width and the weight of the segment (BW) respectively.

Figures 7-9 show the median IDA curves for piers in Table 3. According to each figure, median curves of top drift and normalised based rotation for the piers with no SMA bars A0, B0, and C0, resulted in higher responses compared to the piers with SMA bars. However, the responses for normalised based shear and normalised based moment of the piers without SMA bars follows a lower response due to additional stiffness of the SMA bars.

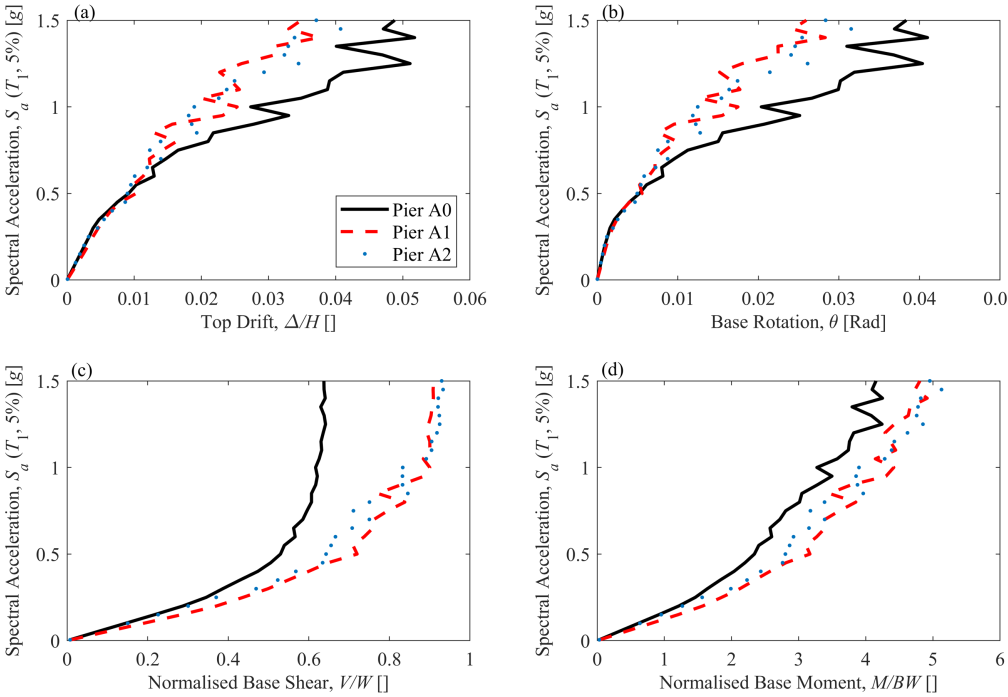

Figure 7. Median IDA curves of all ground motions for the piers A0, A1, and A2: (a) top drift, (b) base rotation, (c) normalised base shear, and (d) normalised base moment.

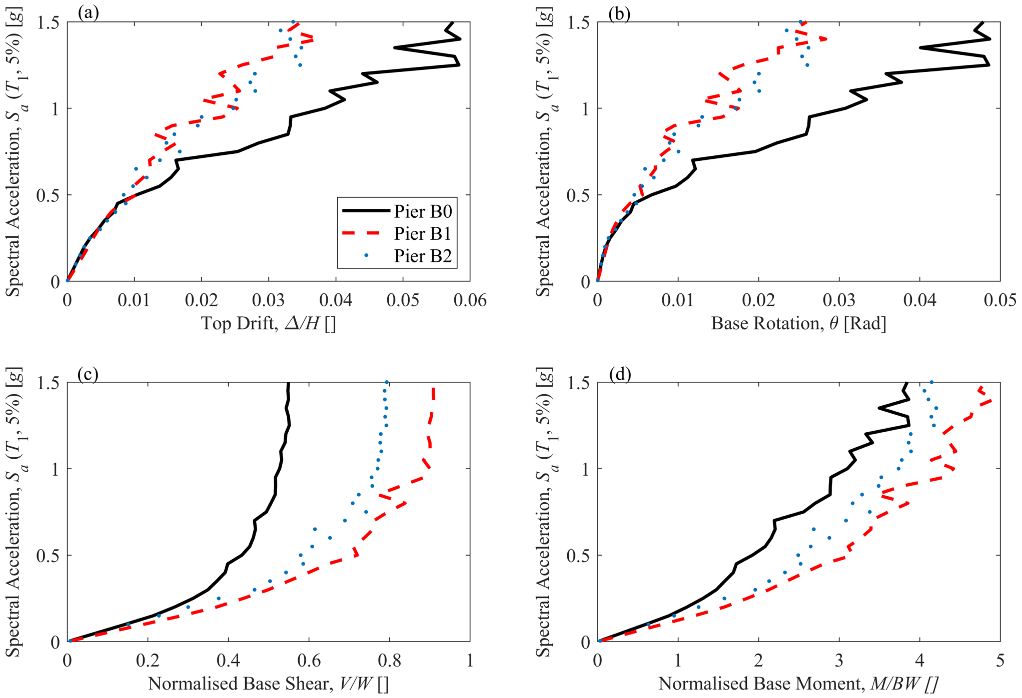

Figure 8. Median IDA curves of all ground motions for the piers B0, B1, and B2: (a) top drift, (b) base rotation, (c) normalised base shear, and (d) normalised base moment.

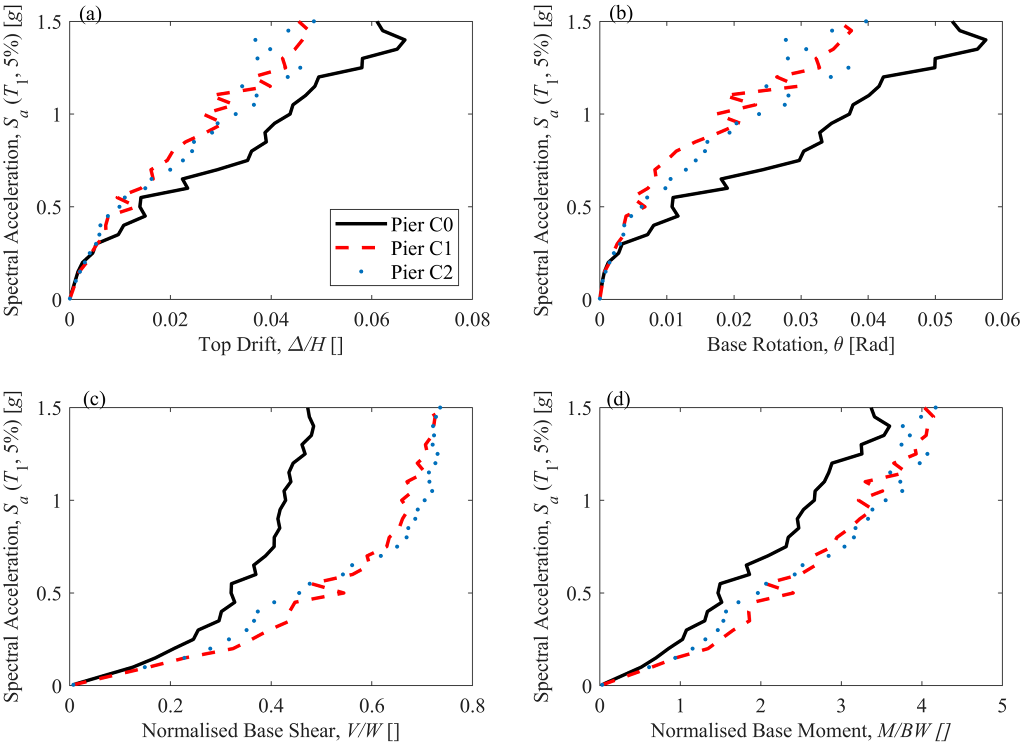

Figure 9. Median IDA curves of all ground motions for the piers C0, C1, and C2: (a) top drift, (b) base rotation, (c) normalised base shear, and (d) normalised base moment.

Figures 10-12 illustrate the IDA curves for all the ground motions along their median curves for piers C0, C1, and C2 for top drift, base rotation, normalised base shear, and normalised base moment. The variation in median curves of each pier with and without SMA bars for top drift and normalised based rotation increases with the increased IM values. However, for normalised base shear and normalised base moment the median curves vary at low IM values at the responses before any gap opening initiated.

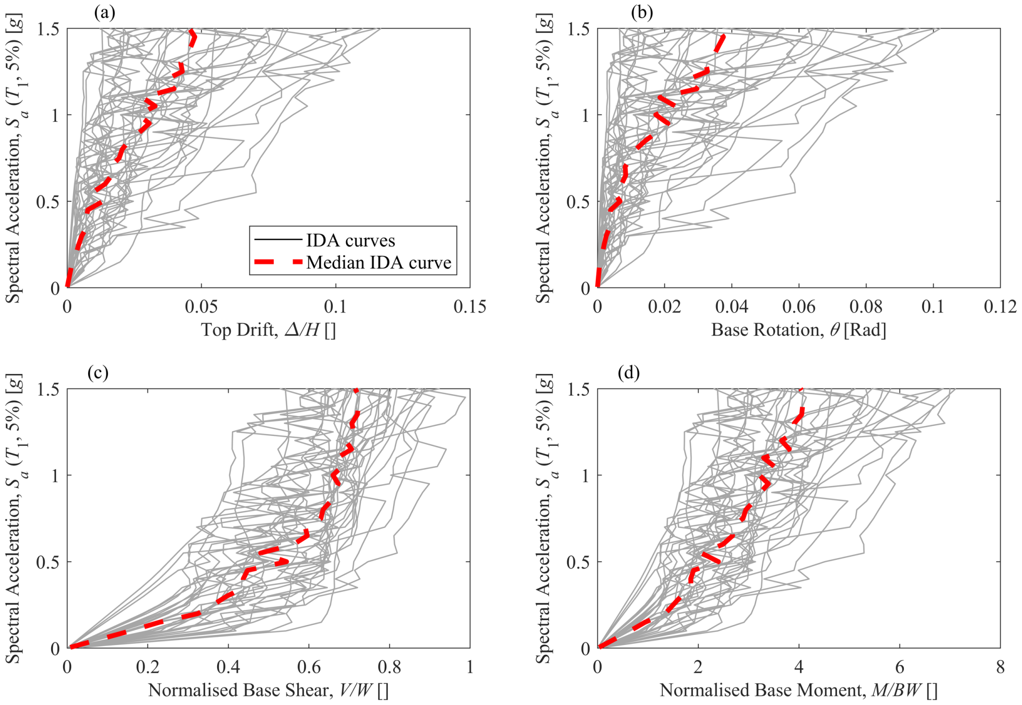

Figure 10. IDA curves and median IDA curves of the pier C1 subject to all ground motions for (a) top drift, (b) base rotation, (c) normalised base shear, and (d) normalised base moment.

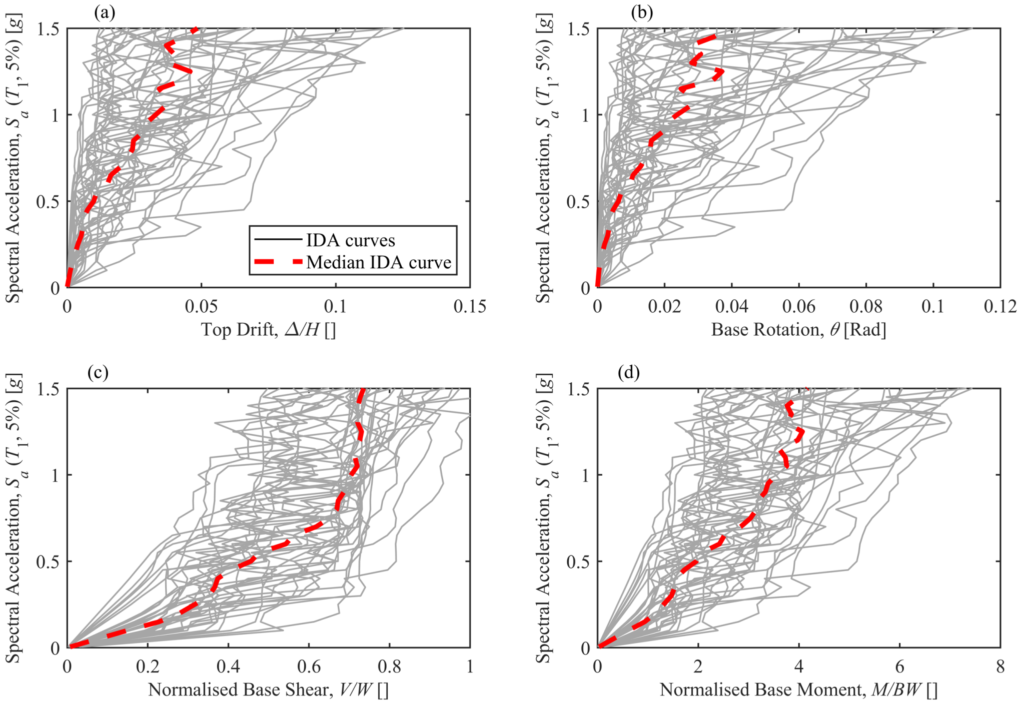

Figure 11. IDA curves and median IDA curves of the pier C2 subject to all ground motions for (a) top drift, (b) base rotation, (c) normalised base shear, and (d) normalised base moment.

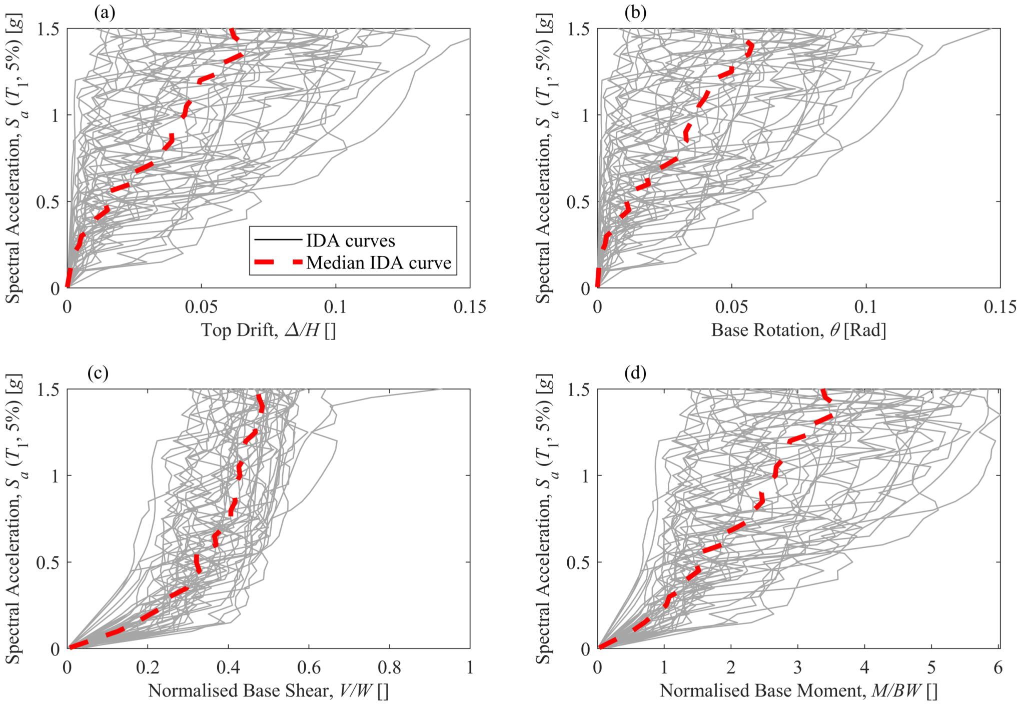

Figure 12. IDA curves and median IDA curves of the pier C0 subject to all ground motions for (a) top drift, (b) base rotation, (c) normalised base shear, and (d) normalised base moment.

Figure 13 showcases the lateral top displacement and corresponding time history for the selected piers when subjected to Component 1 of the Imperial Valley earthquake (refer to Appendix, Table 1). The figures clearly illustrate that the pier without SMA bars, referred to as Pier A0, exhibits higher lateral top displacement in comparison to the piers equipped with SMA bars. This suggests that the incorporation of SMA bars in the piers contributes to a reduction in lateral displacement, thus enhancing their seismic performance.

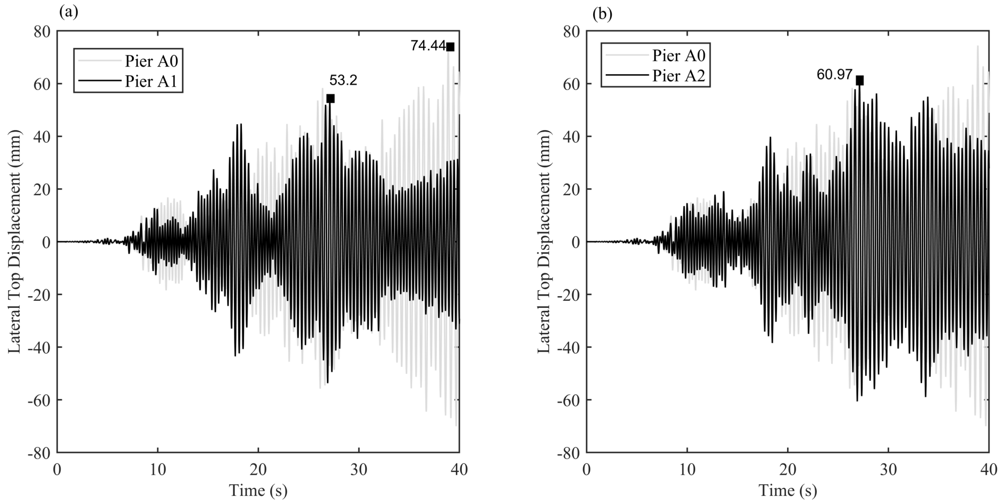

Figure 13. Time history lateral top displacement comparisons for (a) Pier A0 and A1, (b) Pier A0 and A2 subjected to Imperial Valley earthquake.

4.4. Energy Dissipation and Equivalent Viscous Damping

Based on the equations provided in Kashani et al. (2019), the cumulative work done which represents the dissipated energy, is calculated. Figure 14 illustrates the work done by the selected piers equipped with SMA bars when subjected to Component 1 of the Imperial Valley earthquake (refer to Appendix, Table 1).

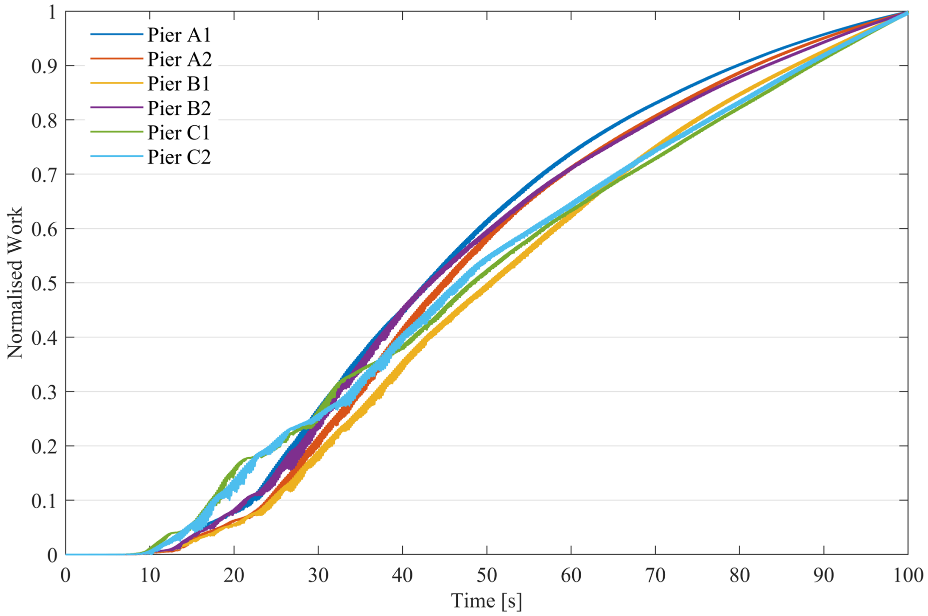

Figure 14. Normalised work for selected piers.

The equivalent viscous damping ratio is determined through a nonlinear static analysis. This analysis involves applying increasing drift amplitudes of 0.5%, 1%, 2%, 3%, 4%, 5%, and 6% cycles, with each cycle being repeated twice. Figure 15 represents the cumulative energy dissipation of selected piers equipped with SMA bars. The equivalent viscous damping ratio of the system is calculated through using the energy dissipation and evaluated via the following equation (Moon et al., 2015; Roh et al., 2012):

$$\xi_{eq} = \frac{E_D}{2\pi K_{eff}\delta_p^2} \; ; \qquad K_{eff} = \frac{V_p - V_n}{\delta_p - \delta_n} \tag{1}$$

where E_D is the energy dissipation per cycle and K_{eff} is the effective stress. The parameters δ_p and δ_n represent the maximum positive and negative displacements, respectively, while V_p and V_n denote the corresponding lateral forces. The figure illustrates the equivalent damping ratio for the specific piers listed in Table 3. Based on the figure, an increase in the initial post-tensioning of the PT tendons leads to a decrease in the ratio of the equivalent viscous damping ratio. Conversely, a higher post-tensioning ratio of the SMA bars results in a higher equivalent viscous damping ratio. The figures clearly indicate that piers without SMA bars, namely A0, B0, and C0, exhibit a zero equivalent viscous damping ratio.

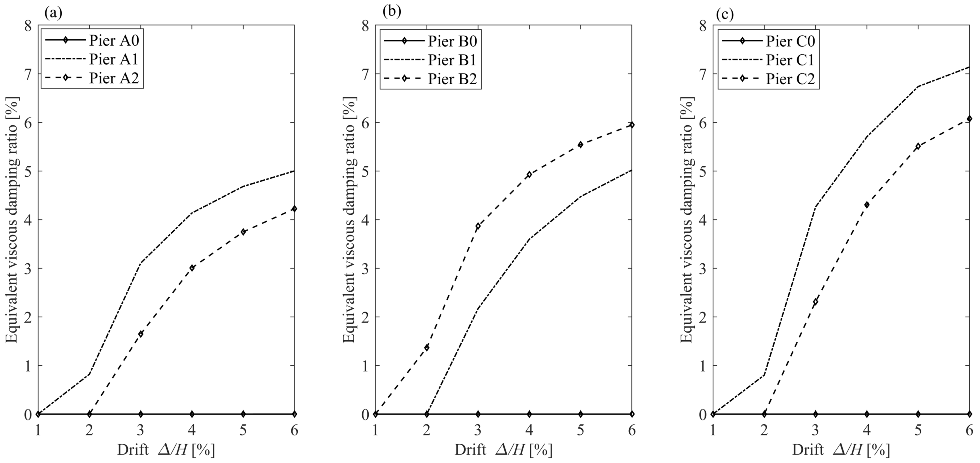

Figure 15. Equivalent damping ratio for selected piers.

5. Conclusions

In this study, seismic performance of PPS bridge piers equipped with SMA bars is examined. An experimentally validated FE model is used to perform numerical analysis of the piers. A parametric study considering nonlinear static analysis is performed for the selected design parameters that might have an influence on the energy dissipation capacity. PPS piers with SMA bars having the highest energy dissipation capacity are chosen to conduct IDA analysis, further, equivalent piers without SMA bars are also analyzed. The IDA results show that SMA bars can significantly reduce the drift responses of the piers. Furthermore, besides providing energy dissipation capacity, SMA bars that are implemented at the bottom of the piers also increase the stiffness of the system. In addition, the future study will concentrate on investigating the seismic performance of PPS piers, considering columns of varying heights on a full scale.

Acknowledgement

The authors acknowledge the support received by the UK Engineering and Physical Sciences Research Council (EPSRC) for a Prosperous Nation [grant number EP/R039178/1]**:** *SPINE:*

Resilience-Based Design of Biologically Inspired Columns for Next-Generation Accelerated Bridge Construction].

References

Ahmadi E and Kashani MM (2020) Numerical investigation of nonlinear static and dynamic behaviour of self-centring rocking segmental bridge piers. *Soil Dynamics and Earthquake Engineering* 128: 105876.

Ahmadi E and Kashani MM (2021) Seismic vulnerability assessment of precast post-tensioned segmental bridge piers subject to far-fault ground motions. *Structures* 34: 2566–2579.

Ahmadi E, Kocakaplan S and Kashani MM (2022) Nonlinear seismic fragility analysis of a resilient precast post-tensioned segmental bridge pier. *Sustainable and Resilient Infrastructure* 7(6): 823–841.

Applied Technology Council (2009) *FEMA P695. Quantification of Building Seismic Performance Factors. 2009.* Applied Technology Council . Available at: https://scholar.google.com/scholar?q=FEMA%20P695.%20Quantification%20of%20Building%20Seismic%20Performance%20Factors.%202009.

Billington SL and Yoon JK (2004) Cyclic Response of Unbonded Posttensioned Precast Columns with Ductile Fiber-Reinforced Concrete. *Journal of Bridge Engineering* 9(4): 353–363.

Billington SL, Barnes RW and Breen JE (1999) A Precast Segmental Substructure System for Standard Bridges. *PCI Journal* 44(4): 56–73.

Chou C-C and Chen Y-C (2006) Cyclic tests of post-tensioned precast CFT segmental bridge columns with unbonded strands. *Earthquake Engineering & Structural Dynamics* 35(2): 159–175.

Dawood H, ElGawady M and Hewes J (2012) Behavior of Segmental Precast Posttensioned Bridge Piers under Lateral Loads. *Journal of Bridge Engineering* 17(5): 735–746.

DesRoches R and Delemont M (2002) Seismic retrofit of simply supported bridges using shape memory alloys. *Engineering Structures* 24(3): 325–332.

Gao N, Jeon J-S, Hodgson DE, et al. (2016) An innovative seismic bracing system based on a superelastic shape memory alloy ring. *Smart Materials and Structures* 25(5): 055030.

Gholampour A and Ozbakkaloglu T (2018) Understanding the compressive behavior of shape memory alloy (SMA)-confined normal- and high-strength concrete. *Composite Structures* 202: 943–953.

Hewes JT and Priestley MJN (2002) *Seismic design and performance of precast concrete segmental bridge columns*. *Rep. No. SSRP-2001/25, Univ. of California San Diego,*. San Diego.

Kashani MM, Ge X, Dietz MS, et al. (2019) Significance of non-stationary characteristics of ground-motion on structural damage: shaking table study. *Bulletin of Earthquake Engineering* 17(9): 4885–4907.

Kocakaplan S, Ahmadi E and Kashani MM (2023) Modelling non-linear dynamic behaviour of rocking bridge piers with shape memory alloys. *Proceedings of the Institution of Civil Engineers - Structures and Buildings*: 1–15.

Lee WK and Billington SL (2010) Modeling Residual Displacements of Concrete Bridge Columns under Earthquake Loads Using Fiber Elements. *Journal of Bridge Engineering* 15(3): 240–249.

Leitner EJ and Hao H (2016) Three-dimensional finite element modelling of rocking bridge piers under cyclic loading and exploration of options for increased energy dissipation. *Engineering Structures* 118: 74–88.

Li C, Hao H and Bi K (2017) Numerical study on the seismic performance of precast segmental concrete columns under cyclic loading. *Engineering Structures* 148: 373–386.

Marriott D, Pampanin S and Palermo A (2009) Quasi-static and pseudo-dynamic testing of unbonded post-tensioned rocking bridge piers with external replaceable dissipaters. *Earthquake Engineering & Structural Dynamics* 38(3): 331–354.

McKenna F (2011) OpenSees: A Framework for Earthquake Engineering Simulation. *Computing in Science & Engineering* 13(4): 58–66.

Moon DY, Roh H and Cimellaro GP (2015) Seismic Performance of Segmental Rocking Columns Connected with NiTi Martensitic SMA Bars. *Advances in Structural Engineering* 18(4): 571–584.

Motaref S, Asce AM, Saiidi MS, et al. (2014) Shake Table Studies of Energy-Dissipating Segmental Bridge Columns. *JOURNAL OF BRIDGE ENGINEERING*: 186–199.

Nikbakht E, Rashid K, Hejazi F, et al. (2015) Application of shape memory alloy bars in self-centring precast segmental columns as seismic resistance. *Structure and Infrastructure Engineering* 11(3): 297–309.

Ou Y-C, Tsai M-S, Chang K-C, et al. (2010) Cyclic behavior of precast segmental concrete bridge columns with high performance or conventional steel reinforcing bars as energy dissipation bars. *Earthquake Engineering & Structural Dynamics* 39(11): 1181–1198.

Roh H and Reinhorn AM (2010) Hysteretic behavior of precast segmental bridge piers with superelastic shape memory alloy bars. *Engineering Structures* 32(10). Elsevier Ltd: 3394–3403.

Roh H, Reinhorn AM and Lee JS (2012) Modeling and cyclic behavior of segmental bridge column connected with shape memory alloy bars. *Earthquake Engineering and Engineering Vibration* 11(3): 375–389.

Shim CS, Chung C-H and Kim HH (2008) Experimental evaluation of seismic performance of precast segmental bridge piers with a circular solid section. *Engineering Structures* 30(12): 3782–3792.

Shrestha B and Hao H (2016) Parametric study of seismic performance of super-elastic shape memory alloy-reinforced bridge piers. *Structure and Infrastructure Engineering* 12(9): 1076–1089.

Suhail R, Amato G and McCrum DP (2020) Active and passive confinement of shape modified low strength concrete columns using SMA and FRP systems. *Composite Structures* 251: 112649.

Tazarv M and Saiid Saiidi M (2016) Low-Damage Precast Columns for Accelerated Bridge Construction in High Seismic Zones. *Journal of Bridge Engineering* 21(3).

Varela S and Saiid' Saiidi M (2014) Dynamic Performance of Novel Bridge columns with superelastic CuAlMn shape memory alloy and ECC. *International Journal of Bridge Engineering* 2(3): 29–58.

Varela S and ‘Saiid’ Saiidi M (2016) A bridge column with superelastic NiTi SMA and replaceable rubber hinge for earthquake damage mitigation. *Smart Materials and Structures* 25(7): 075012.

Wilson JC and Wesolowsky MJ (2005) Shape Memory Alloys for Seismic Response Modification: A State-of-the-Art Review. *Earthquake Spectra* 21(2): 569–601.

Appendix

Table 1. Summary of PEER NGA database information and parameters of recorded far-field ground motions.

	PEER-NGA Record Information

Ground Motion ID	Record Sequence No.	Lowest Frequency (Hz)	Component 1	Component 2	PGA_{max} (g)	PGV_{max} (cm/s)
1	953	0.25	NORTHR/MUL009	NORTHR/MUL279	0.52	63
2	960	0.13	NORTHR/LOS00	NORTHR/LOS270	0.48	45
3	1602	0.06	DUZCE/BOL000	DUZCE/BOL090	0.82	62
4	1787	0.04	HECTOR/HEC000	HECTOR/HEC090	0.34	42
5	169	0.06	IMPVALL/H-DLT262	IMPVALL/H-DLT352	0.35	33
6	174	0.25	IMPVALL/H-E11140	IMPVALL/H-E11230	0.38	42
7	1111	0.13	KOBE/NIS000	KOBE/NIS090	0.51	37
8	1116	0.13	KOBE/SHI000	KOBE/SHI090	0.24	38
9	1158	0.24	KOCAELI/DZC180	KOCAELI/DZC270	0.36	59
10	1148	0.09	KOCAELI/ARC000	KOCAELI/ARC090	0.22	40
11	900	0.07	LANDERS/YER270	LANDERS/YER360	0.24	52
12	848	0.13	LANDERS/CLW-LN	LANDERS/CLW-TR	0.42	42
13	752	0.13	LOMAP/CAP000	LOMAP/CAP090	0.53	35
14	767	0.13	LOMAP/G03000	LOMAP/G03090	0.56	45
15	1633	0.13	MANJIL/ABBAR--L	MANJIL/ABBAR--T	0.51	54
16	721	0.13	SUPERST/B-ICC00	SUPERST/B-ICC090	0.36	46
17	725	0.25	SUPERST/B-POE270	SUPERST/B-POE360	0.45	36
18	829	0.07	CAPEMEND/RIO270	CAPEMEND/RIO360	0.55	44
19	1244	0.05	CHICHI/CHY101-E	CHICHI/CHY101-N	0.44	115
20	1485	0.05	HICHI/TCU045-E	CHICHI/TCU045-N	0.51	39
21	68	0.25	SFERN/PEL090	SFERN/PEL180	0.21	19
22	125	0.13	FRIULI/A-TMZ000	FRIULI/A-TMZ270	0.35	31